geosciences

MDPI

Article

Failure Causes and Kinematics of a Catastrophic Red-Bed Rock Avalanche in Zhenxiong, Yunnan, Southwestern China

Long Yang [1,2], Yueping Yin [1,*] and Sainan Zhu [1]

[1] China Institute of Geo-Environment Monitoring, Beijing 100081, China; yanglong1938@cug.edu.cn (L.Y.); zhusn105@chd.edu.cn (S.Z.)
[2] School of Engineering and Technology, China University of Geosciences (Beijing), Beijing 100083, China
* Correspondence: cug1952@cug.edu.cn

Abstract

At approximately 05:51 on 22 January 2024, a catastrophic red-bed rock avalanche with a volume of 16×10^4 m^3 occurred in Zhenxiong County, Yunnan Province, southwestern China (105°00′47″ E, 27°28′54″ N). The detached rock mass buried 18 houses, killed 44 people, and caused economic losses of 145 million CNY (23.1 million USD). Field investigations, unmanned aerial vehicle (UAV) imagery, interferometric synthetic aperture radar (InSAR) analysis, and two-dimensional discrete-element modelling using PFC2D were conducted to examine the deformation characteristics, failure causes, and kinematics of the rock avalanche. The results show that internal factors, including high-relief terrain resulting from tectonic activity, fractured rock masses caused by joint cutting and weathering, and a soft–hard interbedded stratigraphic structure associated with argillaceous interlayers, were primarily responsible for the failure. Frost heaving may have been an important triggering factor for the Liangshuicun rock avalanche. Continued attention should be paid to slopes around the rock-avalanche site because ground deformation is still ongoing and may lead to future catastrophic events. The numerical simulation reveals that the kinematic process of the rock avalanche from initiation to final deposition lasted approximately 30 s. About 20 s after failure, the rock debris reached the village, burying houses and killing residents. The maximum velocity and displacement of the rock debris were 45 m/s and 335 m, respectively. These findings provide insight into the instability mechanisms and risk assessment of red-bed rock avalanches in the study area.

Keywords: rock avalanche; soft–hard interbedded stratigraphic structure; InSAR; numerical modeling; kinematics

Check for updates

Academic Editor: Salvatore Grasso

Received: 26 April 2026
Revised: 30 June 2026
Accepted: 2 July 2026
Published: 9 July 2026

Copyright: © 2026 by the authors. Licensee MDPI, Basel, Switzerland. This article is an open access article distributed under the terms and conditions of the Creative Commons Attribution (CC BY) license.

1. Introduction

Red beds, consisting of red continental sedimentary clastic rocks and their weathering products, are widely distributed in southwestern China [1,2]. Intense tectonic activity has promoted the development of macro- and micro-scale interfaces in the red beds of this region. As a result, red beds tend to soften and disintegrate under long-term water–rock interaction, creating favourable conditions for landslide development [2].

Zhenxiong County in Yunnan Province is one of the areas most severely affected by geological hazards in southwestern China, largely because of the widespread red beds of the Lower Triassic Feixianguan Formation. For example, on 11 January 2013, a 20×10^4 m^3 rock avalanche occurred in red beds and travelled a horizontal distance of approximately 800 m, destroying Zhaojiagou village and killing 46 people [3]. On 28 January 2013, another

red-bed rock avalanche occurred in Zhongtun Town, Zhenxiong County. Fortunately, because of advance warning, this event caused only economic losses and no fatalities [4]. In June 2014, long-term rainfall triggered a colluvial landslide that destroyed roads, disrupted traffic for two months, and blocked the channel of the Baishui River [5]. These historical disasters have posed serious hazards to the local population and infrastructure.

Many factors, including weathering [6,7], river incision, intense rainfall [8,9], and engineering work [10,11], have been widely recognised as dominant causes of red-bed landslides. Zhang et al. [9] showed that rainfall saturated the sliding zone of the Qingning landslide in southwestern China, significantly increasing pore-water pressure, reducing effective stress, and causing the gently inclined red-bed landslide to fail. Xu et al. [12] concluded that lower dip angles in red beds correspond to higher pore water pressure acting on potential failure surface. Zhang et al. [10] studied a red-bed landslide near the reservoir bank of a hydropower station in southwestern China and concluded that landslide stability deteriorated as water-level oscillations intensified water–rock interaction.

At approximately 05:51 on 22 January 2024, a catastrophic red-bed rock avalanche with a volume of 16×10^4 m^3 occurred in Liangshuicun village, Zhenxiong County, southwestern China, burying 18 houses and killing 44 people in the distal part of its path. Here, we use the Liangshuicun rock avalanche as a case study and analyze its failure causes based on field investigations and InSAR results. Numerical modelling was then conducted to investigate its kinematics. The findings may provide insight into the instability and risk assessment of red-bed rock avalanches in the study area.

2. Geological Setting

The Liangshuicun rock avalanche is located in Zhenxiong County, Yunnan Province, southwestern China (Figure 1). The study area lies at the transition between the northeastern Yunnan–Guizhou Plateau and the upper and middle Yangtze River valley [3]. In this area, elevation decreases from southeast to northwest. The landscape is characterized by deeply incised valleys and steep slopes, typical of the erosional landforms found on the eastern Yunnan Plateau. The local geological architecture is characterised by large- and medium-scale folds, together with torsional and tensional faults [3]. Three normal faults strike NE40–70°, with dips of 65° NW or 45° SE, in the southwestern part of the rock avalanche (Figure 1b).

The study area has a warm and humid subtropical climate controlled by monsoon circulation. The rainy season lasts from June to October, and the freezing period lasts from November to March. Cumulative rainfall during the 20 days before the event was 7.9 mm. The Liangshuicun rock avalanche occurred during the freezing period, when the minimum temperature was −3 °C and snowfall was 0.3 mm (Figure 2).

The local strata are predominantly monoclinal and dip northwestward at angles ranging from approximately 8° to 15° (Figure 1b). The outcrops consist of four geological units: the Quaternary strata (Q_4), the Feixianguan Formation (T_{1f}) of the Lower Triassic, and the Longtan Formation (P_{2l}) and Changxing Formation (P_{2c}) of the Upper Permian. The Quaternary strata (Q_4) consist of colluvial deposits. The Feixianguan Formation (T_{1f}) comprises medium- to thick-bedded siltstone and mudstone intercalated with thin argillaceous interlayers. This formation is highly fractured due to pre-existing tectonic joints and subsequent weathering along these discontinuities, and it hosted the rock avalanche. The Longtan Formation (P_{2l}) comprises medium- to thick-bedded sandstone intercalated with mudstone. This formation contains two mineable coal seams with average thicknesses of 2 m and 1.7 m, respectively. The Changxing Formation (P_{2c}) comprises thin- to medium-bedded sandstone, mudstone, and argillaceous limestone intercalated with a thin coal seam approximately 0.4–0.7 m thick.

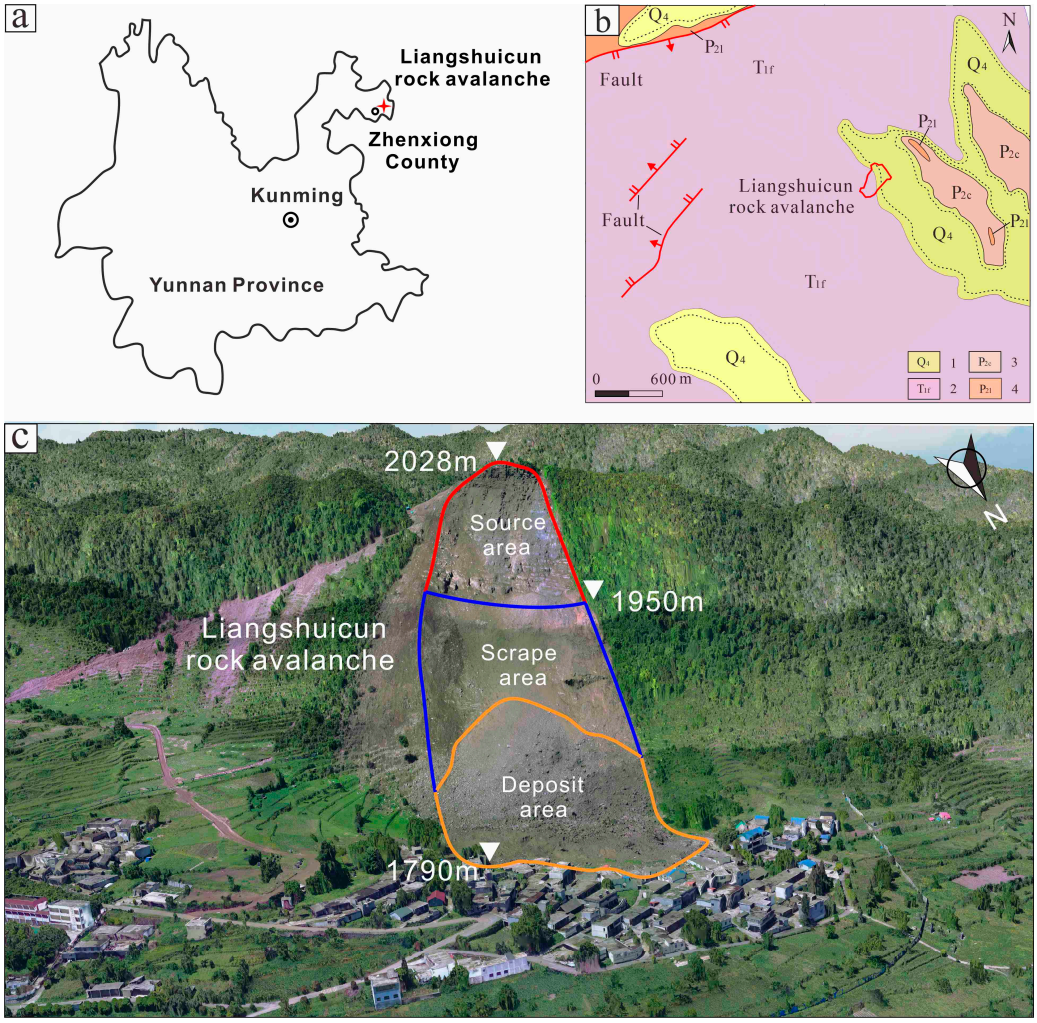


Figure 1. (**a**) Location of the Liangshuicun rock avalanche. (**b**) Regional geological map of the rock avalanche. (1) Quaternary colluvial deposits; (2) Feixianguan Formation, Lower Triassic; (3) Changxing Formation, Upper Permian; (4) Longtan Formation, Upper Permian. (**c**) 3D UAV image of the Liangshuicun rock avalanche.

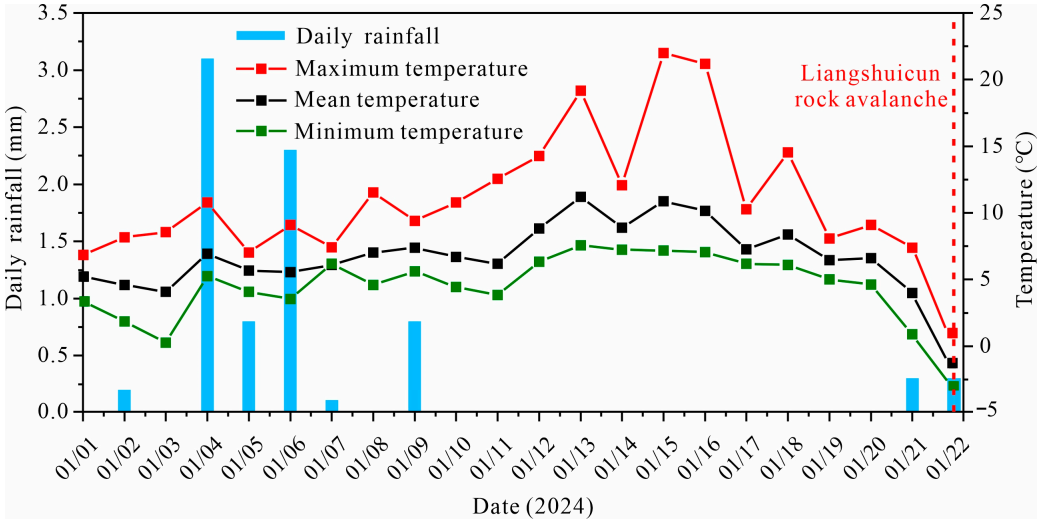


Figure 2. Temperature and rainfall before the Liangshuicun rock avalanche (Tangfang Station).

In the study area, groundwater can be classified, according to occurrence and migration conditions, as pore water, carbonate karst water, and fissure water. In the Quaternary colluvial deposits, pore water is widely present and is derived mainly from rainfall. Fissure water is primarily hosted in joints and weathering fissures in fragmented rocks of the Feixianguan and Longtan Formations. Carbonate karst water occurs mainly in the argillaceous limestone layer of the Changxing Formation.

3. The Liangshuicun Rock Avalanche

The Liangshuicun rock avalanche is located on the northeast limb of the Zhenxiong syncline (105°00′47″ E, 27°28′54″ N). The source area is a cliff with a slope angle of approximately 70°, the scraping zone is a slope with an angle of approximately 40°, and the deposit area is a morphological level with an angle of less than 10° (Figures 1c and 3). The rear of the source area is at an elevation of 2028 m, whereas the toe is at 1790 m. Movement occurred along a direction of N33° E. Between 2028 m and 1950 m elevation, the source zone covers an area of 1.0×10^4 m^2, has an average thickness of 12 m (calculated by interpolating contour lines from pre- and post-event topographic data), and contains a volume of 12×10^4 m^3 (Figures 4 and 5). The total failed volume increased to 16×10^4 m^3 after entraining Quaternary colluvial deposits in the scraping zone along the travel path. The rock debris was finally deposited at elevations ranging from 1860 to 1790 m, burying 18 houses and killing 44 people (Figure 3).



Figure 3. (**a**,**b**) Imagery before and after the Liangshuicun rock avalanche. (**c**,**d**) Rock debris burying houses at the slope toe.

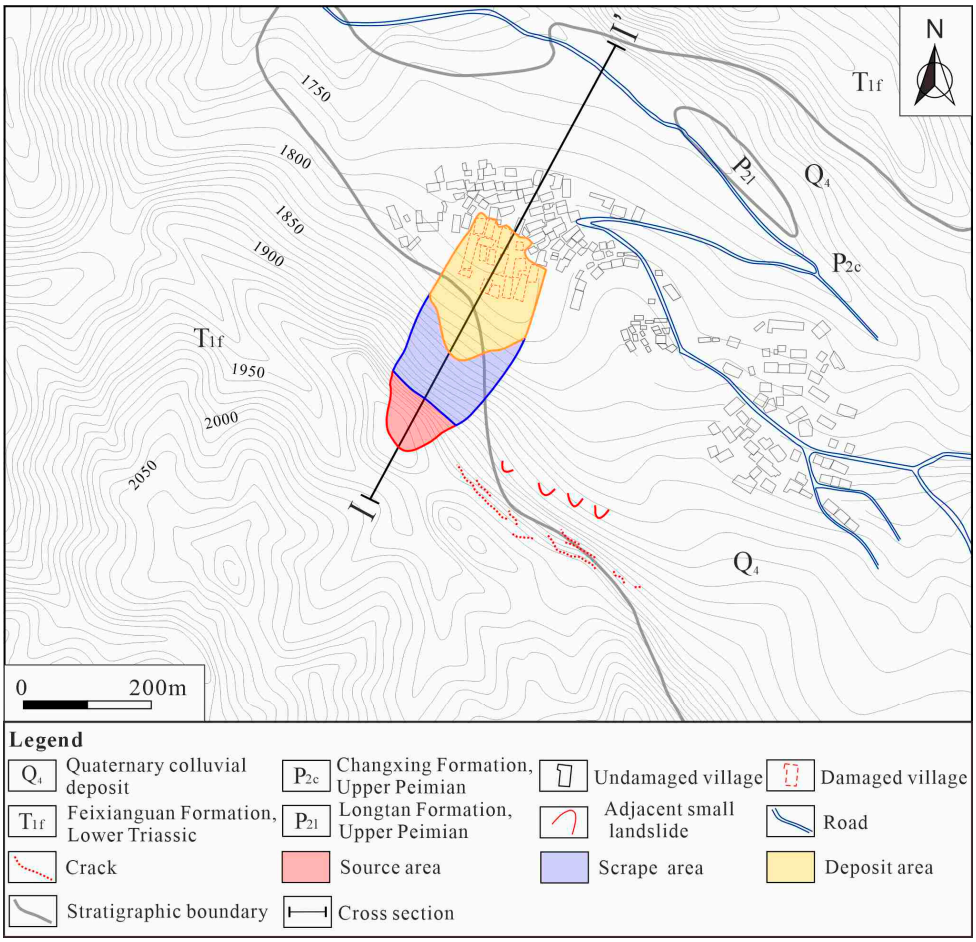


Figure 4. Layout map of the Liangshuicun rock avalanche, showing outcropped strata, rock avalanche boundary, cracks and adjacent small landslides.

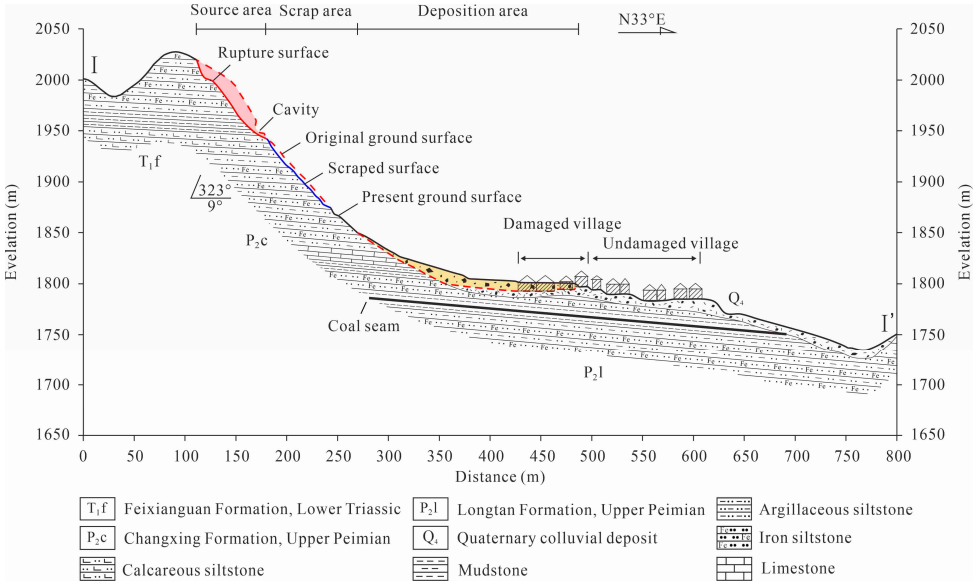


Figure 5. Geological cross section of the Liangshuicun rock avalanche along lines I-I′ shown in Figure 4. The pre-failure ground surface was reconstructed based on pre-event DEM data at 5 m spatial resolution.

A scarp with a slope angle of approximately 70–90° formed at the rock-avalanche headscarp during the failure event (Figure 6a). At the headscarp, medium- to thick-bedded

siltstone and mudstone of the Feixianguan Formation are intercalated with thin argillaceous interlayers 5–15 cm thick and spaced 0.3–1.2 m apart (Figure 6b,c). Three joint sets cut through the exposed rock masses (Figure 6a,b). The first set, with a dip direction of 42° and a dip angle of 78°, runs subparallel to the cliff surface, which strikes approximately NW-SE, and has a spacing of 0.1–4 m. This joint set controls the rupture surface of the rock avalanche, which has a dip direction of 33° and a dip angle of 70° (Figure 6d). The second set has a dip direction of 153° and a dip angle of 84° and is perpendicular to the cliff surface, which strikes approximately NE-SW, with a spacing of 0.1–1 m. The third set corresponds to bedding planes, with a dip direction of 323° and a dip angle of 9°. In the deposit area, boulders ranging from approximately 0.2 to 3 m in size, cut by these three regional joint sets, are chaotically piled together with large voids (Figure 6e). Most of the siltstone and mudstone in the deposit are broken along embedded muddy and sandy strips (Figure 6f). This may have been caused by uneven deformation at material interfaces driven by changes in near-surface moisture and rock-surface temperature [13]. Field investigations in June 2024 identified four new adjacent small landslides around the main rock avalanche (Figures 4 and 7), indicating that the slopes were still deforming five months after the event. These small landslides are spatially adjacent to the main rock avalanche but represent independently developed deformation events.

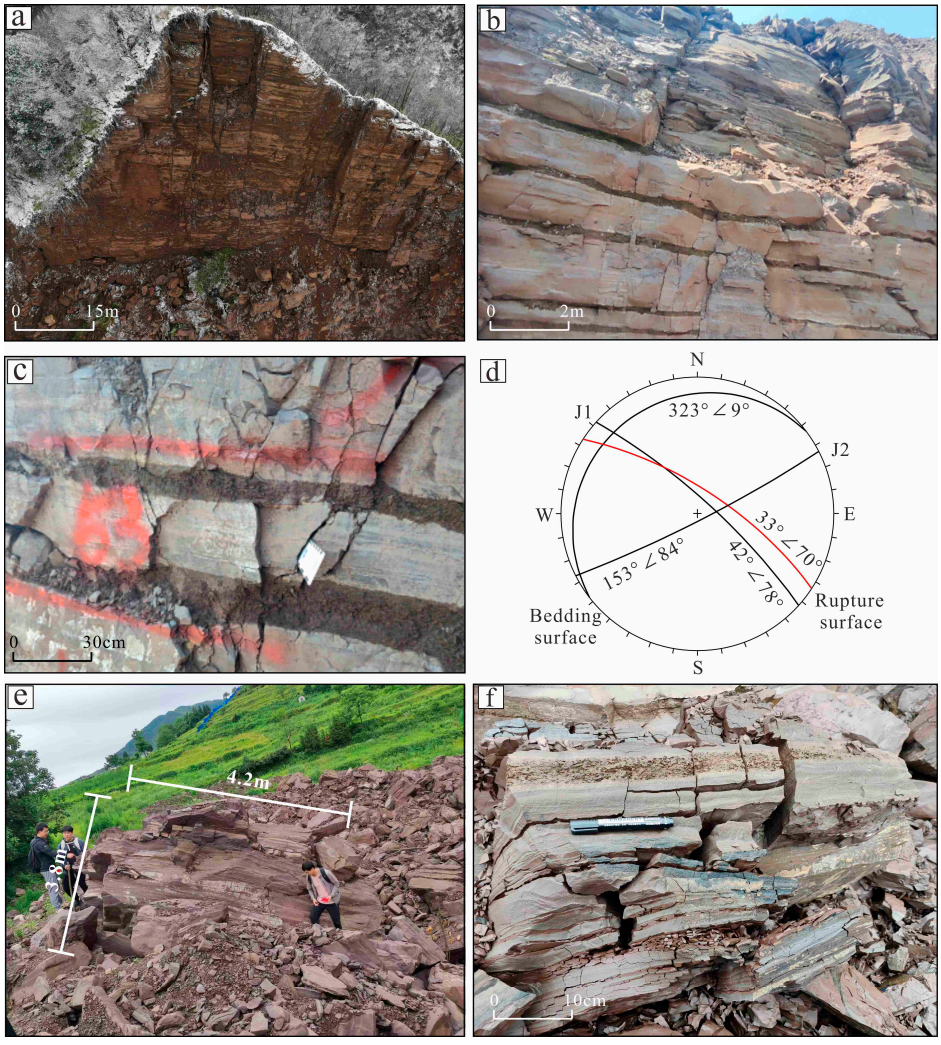


Figure 6. (**a**) Exposed rock masses at the rock-avalanche headscarp. (**b**,**c**) Medium- to thick-bedded siltstone and mudstone intercalated with thin argillaceous interlayers. (**d**) Stereonet of rock-mass discontinuities. (**e**) Boulders in the deposit area. (**f**) Broken siltstone and mudstone.

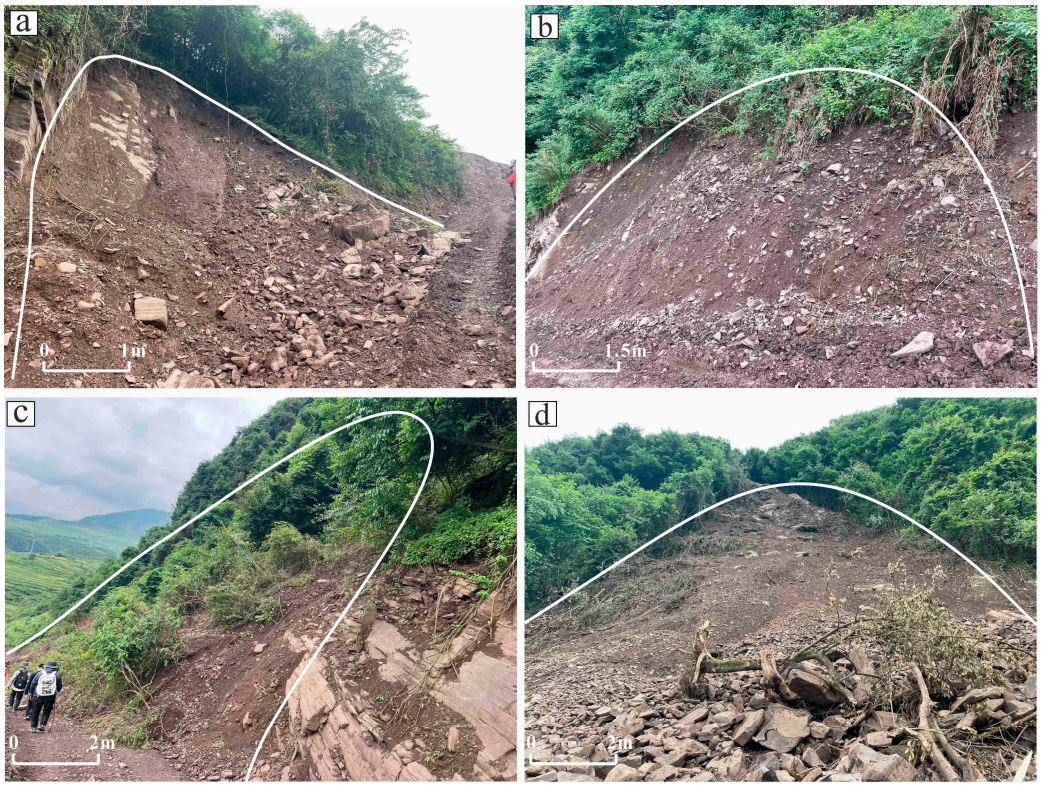


Figure 7. Four adjacent small landslides occurred in June 2024. (**a**) the first; (**b**) the second; (**c**) the third; (**d**) the fourth. The white lines indicate the boundaries of the landslides.

4. Pre-Failure Deformation of the Liangshuicun Rock Avalanche

To detect precursory ground deformation associated with the Liangshuicun rock avalanche, a Sentinel-1A ascending-orbit dataset was used. The dataset had a path number of 128 and an incidence angle of 33.9°, and included 61 Sentinel-1A scenes acquired from 23 April 2022 to 19 January 2024.

Figure 8 shows the pre-failure deformation map of the Liangshuicun rock avalanche. The deformation rate in the rock-avalanche source area was approximately 20 ± 5–100 ± 5 mm/year (Figure 8a). Tensile cracks perpendicular to the sliding direction, with lengths of approximately 36–185 m, widths of approximately 0.1–0.6 m, and visible depths of approximately 0.2–15 m, appeared along the ridge near the source area because of uneven ground deformation (Figure 8b–d). The period of accelerated deformation in the source area corresponded well with the period of decreasing temperature in the study area (Figure 8e).

Notably, the temperature dropped sharply from 4 °C to −3 °C two days prior to the rock avalanche (Figure 2), providing favorable thermal conditions for the freezing of shallow fracture water. Field investigations reveal the presence of bedrock fracture water near the shear outlet, which migrates along structural and bedding fractures and discharges concentratedly at this location. Although the rock mass is generally highly permeable, the presence of multiple mudstone interlayers (5–15 cm thick) and clay-filled discontinuities can act as local aquitards, creating temporary perched water conditions. During cold seasons, infiltrating water resides within these fractures and undergoes water-to-ice phase transition; notably, this freezing does not require a long-term stable groundwater table, as shallow fissure water can freeze rapidly during cold nights and partially thaw during the day. The resultant frost-heaving pressure can further propagate fractures and degrade the rock mass structure. We therefore suggest that seasonal frost-heaving of fracture water near the shear outlet may serve as a contributory factor that aggravates local slope deformation and promotes instability.

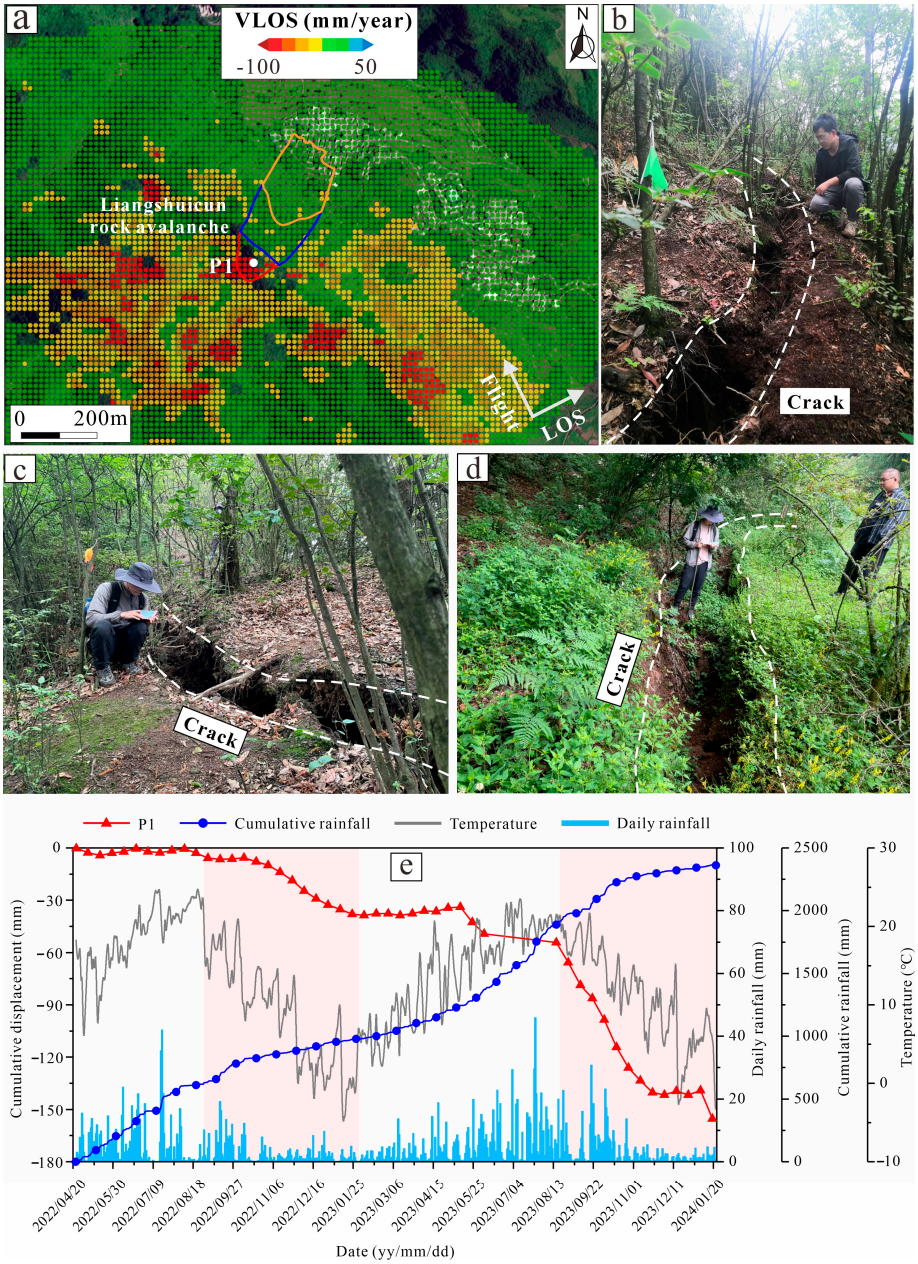


Figure 8. Pre-failure deformation of the Liangshuicun rock avalanche. (**a**) Mean LOS displacement rates superimposed on an optical image. The areas defined by red, blue, and yellow lines are the source, scraping, and deposit areas of the rock avalanche, respectively. P1 is a deformation monitoring point located in the rock-avalanche source area. (**b**–**d**) Tensile cracks. (**e**) Cumulative displacement at P1, daily rainfall, cumulative rainfall, and temperature curves from 23 April 2022 to 19 January 2024. (Negative VLOS values indicate surface displacement away from the satellite along the LOS direction, corresponding to the downslope component of slope movement).

5. Numerical Modeling for the Kinematics of the Rock Avalanche

This study used the two-dimensional particle flow code (PFC 2D, [14]) to simulate the movement process of the Liangshuicun rock avalanche, based on the discrete element method proposed by Cundall and Strack [15]. The code includes two element types: balls, which simulate avalanche material, and walls, which define the model boundaries in this study. A time-stepping algorithm, which cyclically applies Newton's second law to balls and the force-displacement law to contacts, was used to derive the avalanche kinematic parameters.

5.1. Numerical Model

A numerical model of the Liangshuicun rock avalanche was constructed in PFC2D based on the longitudinal section shown in Figure 5 (Figure 9). In the source area, 2944 balls with diameters ranging from 0.1 to 0.3 m were generated to represent the detached rock mass. A total of 15 J1 joints (with a dip direction of 42° and a dip angle of 78°) and 32 bedding planes were introduced to partition this mass into 128 clusters, each measuring 4 × 4 m and distinguished by different colours. The cluster sizes were based on field estimates of the maximum boulder dimensions observed in the deposit. In PFC2D, clusters represent rock masses and break when the applied stress exceeds their shear or tensile strength. In the model, a free boundary was applied at the top, whereas the left, right, and bottom boundaries were fixed, constraining displacements in both the x- and y-directions. The parallel bond model was used in the simulation. This model superimposes a bond component, which resists forces and moments, on a linear elastic component. The bond deforms elastically until the tensile or shear stress exceeds the bond strength, at which point the bond breaks irreversibly and the contact behaves as a linear frictional contact. In addition, 12 monitoring points were placed within the detached rock mass to track velocity and displacement during the simulation (Figure 9). These points were distributed across the rear (M1–M3), middle-upper (M4–M6), middle-lower (M7–M9), and leading (M10–M12) portions of the Liangshuicun rock avalanche.

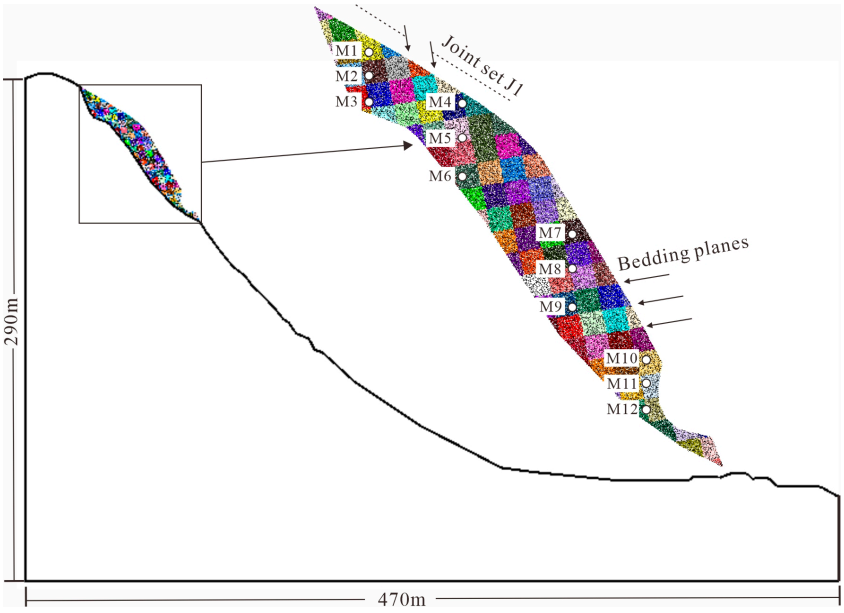


Figure 9. The PFC 2D model of the Liangshuicun rock avalanche. The arrows in the figure are used to indicate the locations of joints.

5.2. Microscale Properties of Balls and Contacts

Uniaxial compression tests were carried out in the laboratory on siltstone samples from the Feixianguan Formation at the Liangshuicun rock-avalanche site. The resulting macroscale strength and deformation parameters were an unconfined compressive strength (UCS) of 121.2 MPa, Young's modulus (E) of 22.1 GPa, and Poisson's ratio (v) of 0.24. To establish the relationship between material properties and numerical parameters, a series of numerical uniaxial compression tests replicating the laboratory procedures was performed (Figure 10). Using the microscale parameters listed in Table 1, the numerical model (Figure 10) yielded UCS, E, and v values that closely matched the laboratory test results. This close agreement indicates that the selected microparameters can reproduce the behaviour of the Liangshuicun rock-avalanche material satisfactorily (Table 1). For balls

and bonds along joints and bedding planes, the parameters were assigned half the values used for intact siltstone [16]. A high normal stiffness value of 3×10^{10} was adopted for ball-wall contacts to prevent balls from penetrating walls during model construction. To model energy dissipation during rock-avalanche motion [15], the damping coefficient was set to 0.01 [16].

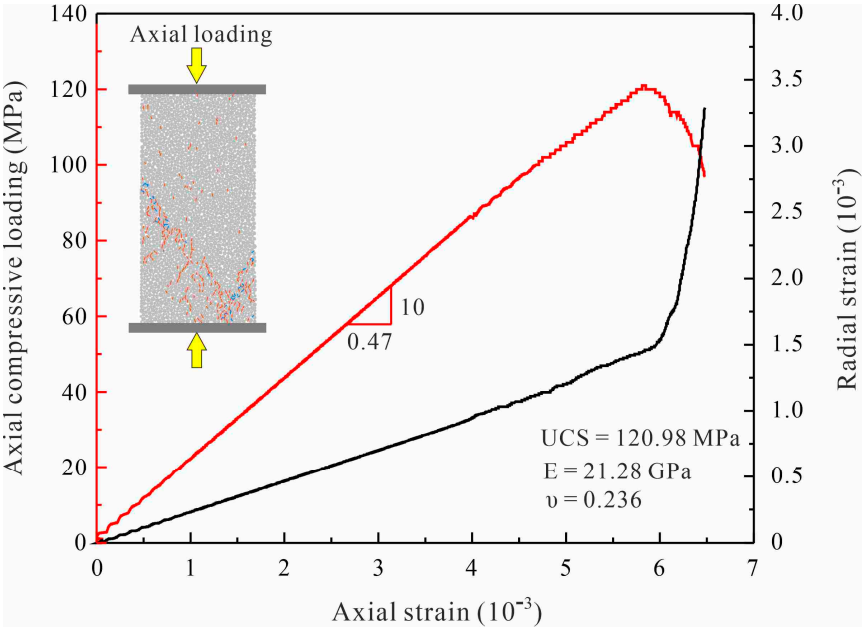


Figure 10. Results from numerical uniaxial compression testing.

Table 1. Micro-properties of balls composing the rock material in the numerical model.

Parameters	Description	Value
R_{min}	Minimum particle radius (m)	0.1
R_{max}	Maximum particle radius (m)	0.3
ρ	Particle density (kg/m^3)	2350
μ	Friction coefficient	0.4
E_c	Effective modulus (GPa)	1.94
K	Normal-to-shear stiffness ratio	0.185
T	Tensile strength (MPa)	206
C	Cohesion (MPa)	64
θ	Friction angle (°)	38

5.3. Calibration of the Numerical Model

The friction coefficient of the transport path was used to calibrate the Liangshuicun numerical model until the simulated displacement and final deposit distribution approached the field observations [16]. To reproduce the movement of the rock avalanche, five coefficients (0.8, 0.4, 0.35, 0.3, and 0.2) were assigned to the transport path. Figure 11 shows the calibration results for these friction coefficients. When the friction coefficient was set to 0.35 or higher, the rock debris accumulated mainly near the slope toe, and the simulated displacement substantially underestimated the field measurements. When the friction coefficient was less than 0.3, the simulated displacement was close to the observed value, but most of the rock debris was deposited at the distal end of the path. When the friction coefficient was 0.3, the modelling results were broadly consistent with the observed dis-

placement and deposit distribution (Figure 5). Therefore, 0.3 was adopted as the friction coefficient of the transport path.

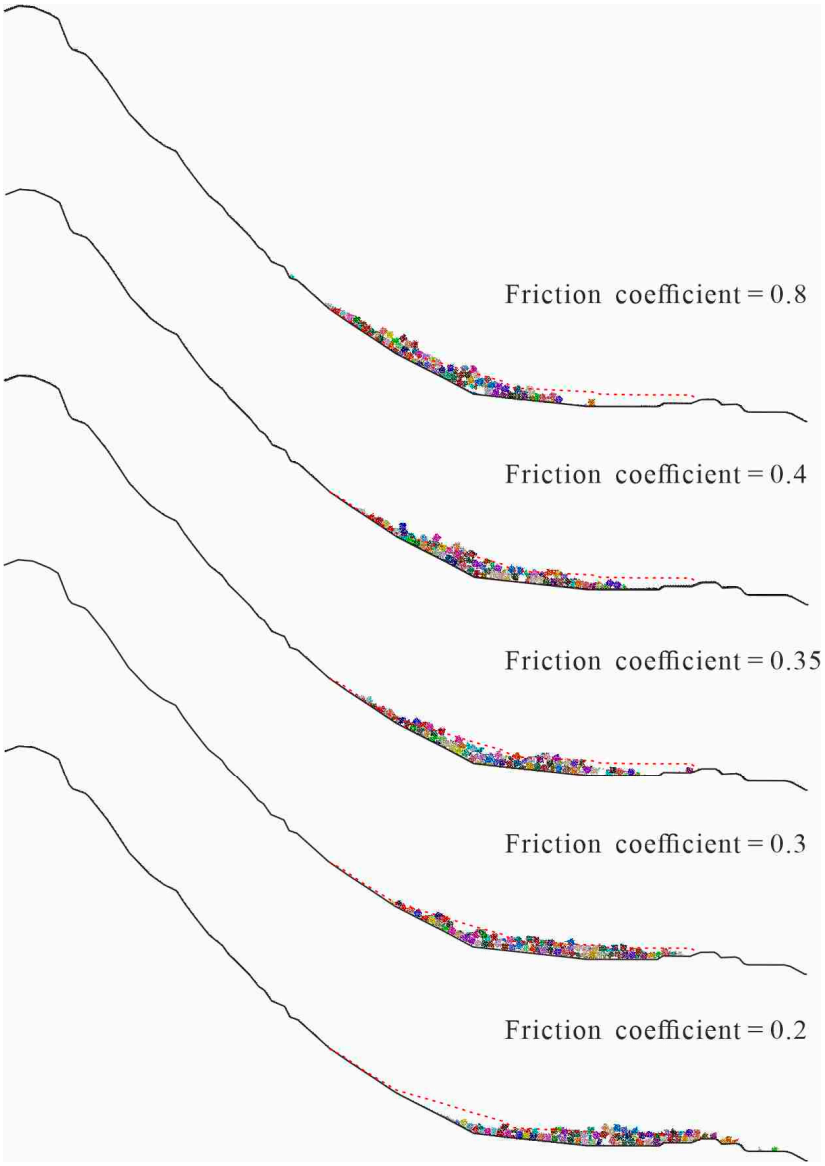


Figure 11. Calibration results for different friction coefficients of the transport path of the Liangshuicun rock avalanche. The red dotted line indicates the post-event topography.

5.4. Modeling Results

Figure 12 shows the simulated kinematics of the Liangshuicun rock avalanche using PFC2D. The simulation results show that failure initiated at the front of the detached rock mass and then propagated to the middle and rear sections as anti-sliding resistance was lost, ultimately leading to complete failure of the entire rock mass. At t = 2 s, the detached mass slid off the toe of the rupture surface and was then launched into the air along a parabolic trajectory (t = 5 s). While airborne, the rock mass fragmented into blocks bounded by two joint sets. After violent impact with the ground, the material broke down further into rock debris. After collision, gravitational potential energy was converted into kinetic energy, causing the debris to roll rapidly downslope (t = 10 s). By t = 20 s, the rock debris had reached the village, burying houses and causing fatalities. Eventually, the kinetic energy was fully dissipated, bringing the debris to rest. The final deposit matched the observed field deposit well (t = 30 s).

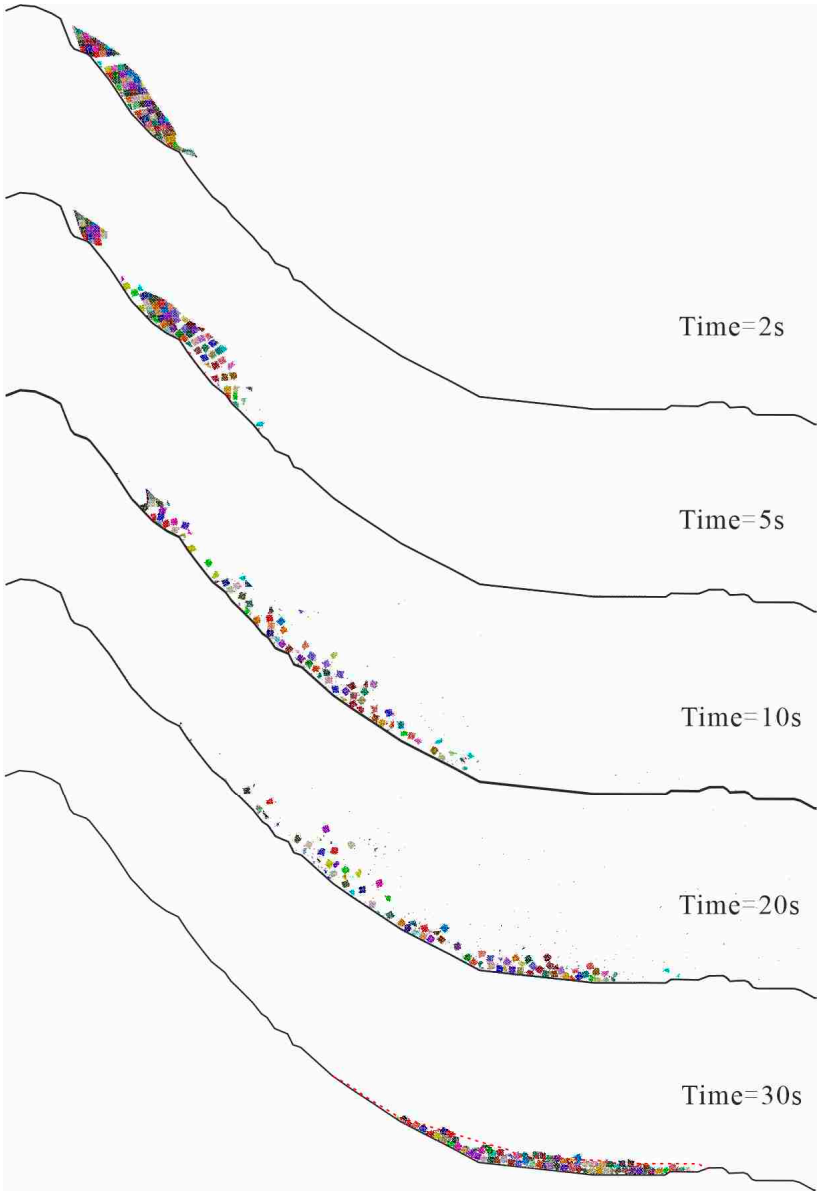


Figure 12. Movement behavior of the Liangshuicun rock avalanche. The post-event terrain is indicated by the red dashed line.

Figure 13 shows velocity–time curves for the rear (a), middle-upper (b), middle-lower (c), and leading (d) parts of the Liangshuicun rock avalanche. The velocities of all four parts increased rapidly to peak values during the initial 8–13 s and then decreased to less than 0.1 m/s during the following 17–22 s. The peak velocities of the rear, middle-upper, middle-lower, and leading parts were 36 m/s, 35 m/s, 37 m/s, and 45 m/s, occurring at 13 s, 12 s, 12 s, and 9 s, respectively. The leading part reached a higher peak velocity earlier than the rear part, indicating that failure initiated earlier in the leading part than in the rear part.

Figure 14 shows displacement–time curves for four sections of the Liangshuicun rock avalanche: rear (a), middle-upper (b), middle-lower (c), and leading (d). In all four sections, displacement increased rapidly at the beginning, then increased more slowly, and eventually levelled off. Maximum displacements reached 332 m at the rear, 321 m at the middle-upper section, 328 m at the middle-lower section, and 335 m at the leading section of the sliding mass. The times required for displacement to stabilise ranged from approximately 20–24 s for the rear, 20–23 s for the middle-upper section, 17–20 s for the

middle-lower section, and 16–18 s for the leading section. These timing differences indicate that the rear section moved later than the front section.

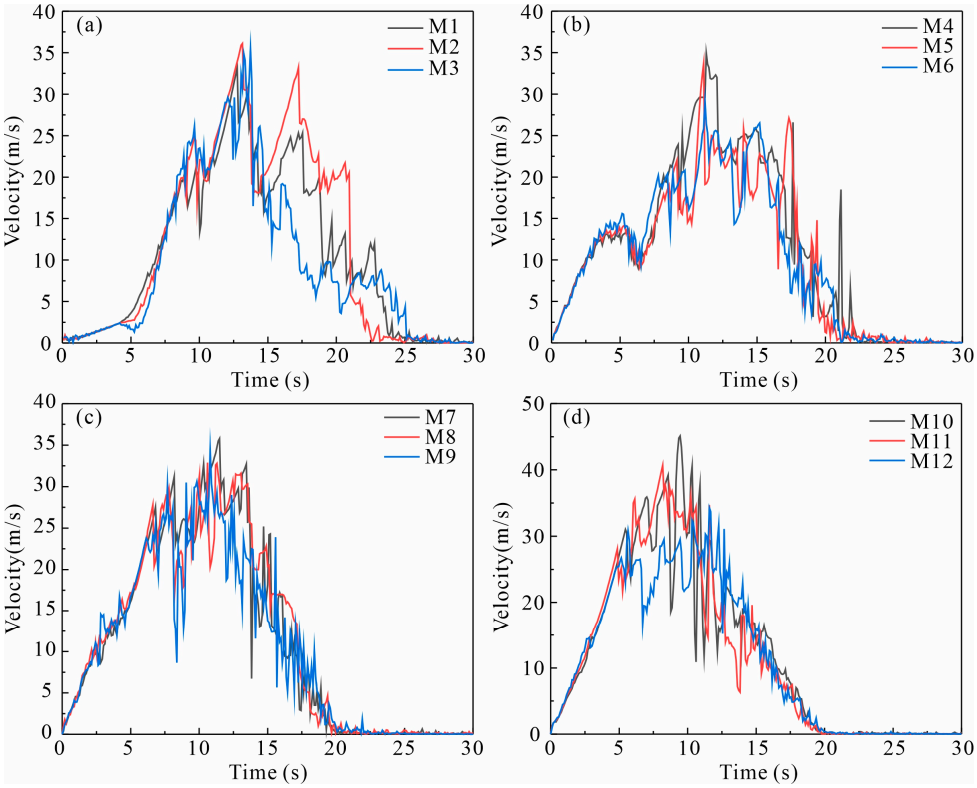


Figure 13. Velocity–time curves for the rear (**a**), middle-upper (**b**), middle-lower (**c**), and leading (**d**) parts of the Liangshuicun rock avalanche.

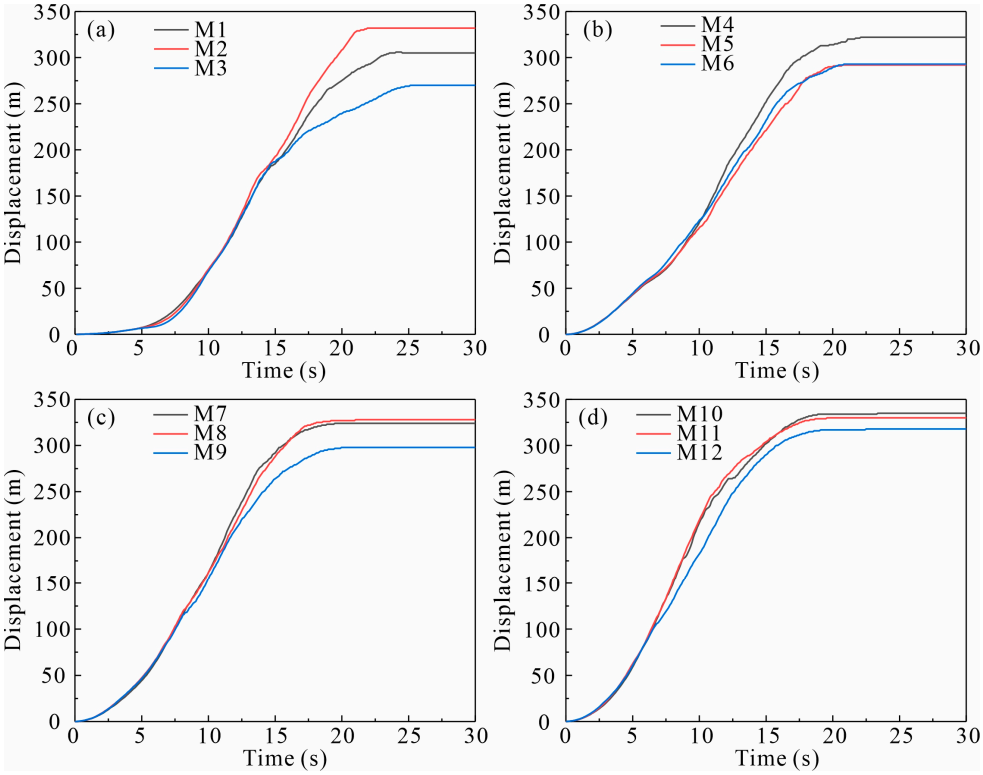


Figure 14. Displacement–time curves for the rear (**a**), middle-upper (**b**), middle-lower (**c**), and leading (**d**) parts of the Liangshuicun rock avalanche.

6. Discussion

6.1. Failure Causes of the Liangshuicun Rock Avalanche

The detached rock masses consisted of medium- to thick-bedded siltstone and mudstone intercalated with thin argillaceous interlayers of the Feixianguan Formation (Figure 6). Siltstone and mudstone can break along cracks formed by uneven expansion and/or contraction at interfaces between different materials under oscillations in near-surface moisture and rock-surface temperature [13,17]. This interpretation is supported by field evidence showing that most siltstone and mudstone in the deposit were broken along embedded muddy and sandy strips (Figure 6f). The thin argillaceous interlayers resulted from long-term chemical water–rock interaction in claystone [18–20]. Groundwater in the study area drained and migrated preferentially along bedding planes and joint networks, providing long-lasting and stable fluid pathways for water–rock reactions. Field evidence of argillaceous interlayers at the rock-avalanche headscarp indicates that water–rock interaction occurred not only on the rock surface but also deep within the rock mass. At least the claystone buried at depths of approximately 10–15 m in the detachment zone had been completely argillized before the event (Figures 5 and 6), indicating that prolonged groundwater flow along bedding-parallel structures significantly facilitated the deep chemical alteration of claystone. The soft–hard interbedded structure of the rock mass is generally considered unfavorable for slope stability [21,22]. In this case, the bedding planes and joint sets within the Feixianguan Formation acted as mechanical discontinuities that reduced the overall shear strength of the rock mass and provided preferential pathways for groundwater infiltration. Over time, water–rock interactions along these discontinuities further weakened the rock mass through progressive degradation. This structural setting thus defined the boundary conditions that ultimately facilitated the initiation of the rock avalanche.

The cracks (Figure 8) and fractured rock masses (Figure 6) caused by joint cutting and weathering before the Liangshuicun rock avalanche facilitated rainfall infiltration and storage. More importantly, a water-collecting depression developed at the rear scarp effectively concentrated atmospheric precipitation and funneled it into the fracture network, significantly enhancing local groundwater recharge (Figure 5). Field investigations indicate that groundwater in the study area is primarily recharged by rainfall, infiltrating downward along high-angle joints and being impeded by relatively impermeable layers (particularly above the mudstone interlayers), thereby creating local hydrostatic pressure conditions. We therefore infer that fissure water was widely distributed in the detached rock masses. Notably, the shear outlet of the landslide coincided with a discharge point of fracture water, where groundwater seeped continuously along bedding planes and joint networks—even during periods of low rainfall—indicating a persistent groundwater flow system within the slope. Given the limited extent of the study area (source area of approximately 1.0×10^4 m^2), the groundwater flow system is relatively small in scale and can be considered as locally hydrostatic rather than regional dynamic conditions. This inference is also supported by field evidence of wet argillaceous interlayers at the rock-avalanche headscarp (Figure 6c).

The sharp temperature drop from 4 °C to −3 °C before the event (Figure 2) suggests that shallow fissure water (within a few meters of the surface) may have frozen into ice. It should be noted that water seepage at the shear outlet is characterized by slow seepage/dripping rather than rapid flow, which allows shallow fissure water to undergo localized freezing during cold nights when temperatures drop sharply. Freezing of shallow fissure water can produce several to tens of megapascals of frost-heaving stress inside rock masses [23]. Although this shallow freeze–thaw action does not directly affect the deep failure surface, it can progressively extend shallow cracks through repeated freeze–thaw cycles and exacerbate rock mass deterioration, thereby promoting increased deformation

activity and even instability in rock avalanches [3,24,25]. The effect of freeze–thaw on slope stability is dualistic: under certain conditions, ice can temporarily act as a cementing agent that reinforces the rock mass; however, during freeze–thaw cycles, the fatigue effect induced by repeated water-ice phase transitions ultimately leads to the deterioration of rock mass structure, rather than the immediate effect of a single freezing event. This may explain why the period of accelerated deformation in the source area corresponded well with the period of decreasing temperature (Figure 8e). We therefore suggest that frost heaving may have been one of the key factors triggering the Liangshuicun rock avalanche.

It is worth noting that new adjacent small landslides developed around the rock-avalanche site after the event (Figure 7), indicating that ground deformation was still ongoing five months later. Continued attention should therefore be paid to these slopes to reduce the risk of future catastrophic events.

6.2. Kinematics of the Rock Avalanche

The transport process of the Liangshuicun rock avalanche can be described as follows. After failure, the detached rock masses moved off the toe of the rupture surface and were launched into the air along a parabolic trajectory. While airborne, the material fragmented into blocks bounded by two joint sets and then broke further into debris after violent impact with the ground. At the same time, approximately 4×10^4 m^3 of loose soil along the travel path was incorporated into the rock debris because of the substantial kinetic energy involved. About 20 s after failure, the rock debris reached the village, burying houses and killing residents. Eventually, the debris stopped moving after its kinetic energy was dissipated. Overall, the kinematic process from initiation to final deposition lasted approximately 30 s. The maximum velocity and displacement of the rock debris were 45 m/s and 335 m, respectively.

7. Conclusions

A preliminary investigation of the catastrophic red-bed Liangshuicun rock avalanche in Zhenxiong County, Yunnan Province, southwestern China, was conducted. The deformation characteristics, failure causes, and kinematics were analysed in detail. The following conclusions were drawn:

1. High-relief terrain, fractured rock masses caused by joint cutting and weathering, and a soft–hard interbedded stratigraphic structure associated with argillaceous interlayers were the main internal factors contributing to the Liangshuicun rock avalanche.
2. Frost heaving may have been an important triggering factor for the Liangshuicun rock avalanche. Continued attention should be paid to slopes around the rock-avalanche site because ground deformation is still ongoing and may lead to future catastrophic events.
3. The movement process of the rock avalanche from initiation to final deposition lasted approximately 30 s. About 20 s after failure, the rock debris reached the village, burying houses and killing residents. The maximum velocity and displacement of the rock debris were 45 m/s and 335 m, respectively.

Author Contributions: L.Y.: Investigation, Conceptualization, Methodology, Writing. Y.Y.: Investigation, Editing, Funding acquisition. S.Z.: Investigation, Data curation. All authors have read and agreed to the published version of the manuscript.

Funding: This study was supported by the National Natural Science Foundation of China (Grant No. U2244227), the National Key R&D Program of China (Grant No. 52130905), and the Yunnan Provincial Science and Technology Department (Contract No. 202403AA080001).

Data Availability Statement: The original contributions presented in this study are included in the article. Further inquiries can be directed to the corresponding author.

Acknowledgments: The authors thank Jiansong Shi, Limei Zhang, Yaqi Shen, and Feng Gao for their technical assistance and support with data collection.

Conflicts of Interest: The authors declare no conflicts of interest.

References

1. Yin, Y.P.; Huang, B.L.; Zhang, Q.; Yan, G.Q.; Dai, Z.W. Research on recently occurred reservoir-induced Kamenziwan rockslide in Three Gorges Reservoir, China. *Landslides* **2020**, *17*, 1935–1949. [CrossRef]
2. Leng, Y.Y.; Kong, X.Z.; He, J.Y.; Xing, A.G.; Zhang, Y.B.; Wang, Q. The July 10, 2020, red-bed landslide triggered by continuous rainfall in Qianxi, Guizhou, China. *Landslides* **2022**, *19*, 1421–1433. [CrossRef]
3. Yin, Y.P.; Xing, A.G.; Wang, G.H.; Feng, Z.; Li, B.; Jiang, Y. Experimental and numerical investigations of a catastrophic long-runout landslide in Zhenxiong, Yunnan, Southwestern China. *Landslides* **2017**, *14*, 649–659. [CrossRef]
4. Xu, Y.Q.; Yin, Z.Q.; Zhang, N.; Sa, L.P. Analysis of the cause of Toutun large scale landslide in Zhenxiong County, Yunnan Province. *Chin. J. Geol. Hazard Control* **2015**, *26*, 6–11+24. (In Chinese)
5. Yin, Z.Q. Accumulation landslide in Luokan village, Zhenxiong Zhenfeng second-class highway, Zhaotong City, Yunnan Province. *Chin. J. Geol. Hazard Control* **2015**, *26*, 42. (In Chinese)
6. Wang, G.L.; Wang, T.G.; Han, K.Y.; Wang, L.S.; Shi, S.B. Recognition of a novel Precambrian petroleum system based on isotopic and biomarker evidence in Yangtze platform, South China. *Mar. Pet. Geol.* **2015**, *68*, 414–426. [CrossRef]
7. Zhang, C.; Yu, C.; Leung, A.K.; Mohammad, S.; Choi, C.E. Uprooting dynamics of a model tree under rockfall impact: Combined experimental and numerical insights. *Earth Surf. Process. Landf.* **2025**, *50*, e70114. [CrossRef]
8. Yamagishi, H. Recent Landslides in Western Hokkaido, Japan. *Pure Appl. Geophys.* **2000**, *157*, 1115–1134. [CrossRef]
9. Zhang, M.; Yin, Y.P.; Huang, B.L. Mechanisms of rainfall-induced landslides in gently inclined red beds in the eastern Sichuan Basin, SW China. *Landslides* **2015**, *12*, 973–983. [CrossRef]
10. Zhang, H.; Hu, Z.Q.; Ma, B.; Chen, X.Z. Stability analysis of a red bed slope reservoir bank considering water-rock interaction characteristics. *Desalin. Water Treat.* **2021**, *239*, 289–300. [CrossRef]
11. Du, J.T.; Song, C.; Li, Z.H.; Tomás, R.; Li, Z. Kinematic behavior and sliding geometry of large anthropogenic-induced landslides using three-dimensional time series InSAR: Insights from the likan road landslide. *Landslides* **2025**, *22*, 3319–3333. [CrossRef]
12. Xu, Q.; Huang, R.; Liu, T.; Fan, X.; Ge, H.; Song, X. Study of the formation mechanism and design of control engineering for the super-huge Tiantai landslide, Sichuan Province, China. In *IAEG 2006 Engineering Geology for Tomorrow Cities*; Geological Society of London: London, UK, 2006; p. 602.
13. Lamp, J.L.; Marchant, D.R.; Mackay, S.L.; Head, J.W. Thermal stress weathering and the spalling of Antarctic rocks. *J. Geophys. Res. Earth Surf.* **2017**, *122*, 3–24. [CrossRef]
14. Itasca Consulting Group. *Particle Flow Code in 2 Dimensions (Version 5.0)*; Itasca Consulting Group: Minneapolis, MN, USA, 2014.
15. Cundall, P.A.; Strack, O. Discussion: A discrete numerical model for granular assemblies. *Géotechnique* **1980**, *30*, 331–336. [CrossRef]
16. Zhang, M.; Wu, L.Z.; Zhang, J.C.; Li, L.P. The 2009 Jiweishan rock avalanche, Wulong, China: Deposit characteristics and implications for its fragmentation. *Landslides* **2019**, *16*, 893–906. [CrossRef]
17. Zhou, C.Y.; Liu, C.H.; Liang, Y.H.; Liu, Z.; Wei, P.C.; Wang, X.D. Application of natural weathered red-bed soil for effective wall protection filter-cake formation. *Mater. Lett.* **2020**, *258*, 126679. [CrossRef]
18. Gupta, V.; Ahmed, I. The effect of pH of water and mineralogical properties on the slake durability (degradability) of different rocks from the Lesser Himalaya, India. *Eng. Geol.* **2007**, *95*, 79–87. [CrossRef]
19. Koralegedara, N.H.; Maynard, J.B. Chemical, mineralogical and textural properties of the Kope Formation mudstones: How they affect its durability. *Eng. Geol.* **2017**, *228*, 312–322. [CrossRef]
20. Baldermann, A.; Dietzel, M.; Reinprecht, V. Chemical weathering and progressing alteration as possible controlling factors for creeping landslides. *Sci. Total Environ.* **2021**, *778*, 146300. [CrossRef] [PubMed]
21. Li, S.; Li, X.; Zhang, N.; Liao, Q. Sedimentation characteristics of the Jurassic sliding-prone stratum in the Three Gorges reservoir area and their influence on physical and mechanical properties of rock. *J. Eng. Geol.* **2004**, *12*, 385–389. [CrossRef]
22. Liu, H.D.; Liu, C.Y.; Yue, X.; Wang, J. Study on mechanical properties and acoustic emission characteristics of mudstone-clay composites under uniaxial compression. *Eng. Geol.* **2024**, *332*, 107478. [CrossRef]
23. Wen, T.; Chen, N.S.; Huang, D.X.; Wang, Y.K. A medium-sized landslide leads to a large disaster in Zhenxiong, Yunnan, China: Characteristics, mechanism and motion process. *Landslides* **2025**, *22*, 3365–3383. [CrossRef]
24. Deline, P.; Akcar, N.; Ivy-Ochs, S.; Kubik, P.W. Repeated Holocene rock avalanches onto the Brenva Glacier, Mont Blanc Massif, Italy: A chronology. *Quat. Sci. Rev.* **2015**, *126*, 186–200. [CrossRef]

25. Calamita, G.; Gallipoli, M.R.; Gueguen, E.; Sinisi, R.; Summa, V.; Vignola, L.; Stabile, T.A.; Bellanova, J.; Piscitelli, S.; Perrone, A. Integrated geophysical and geological surveys reveal new details of the large Montescaglioso (Southern Italy) landslide of December 2013. *Eng. Geol.* **2023**, *313*, 106984. [CrossRef]

Disclaimer/Publisher's Note: The statements, opinions and data contained in all publications are solely those of the individual author(s) and contributor(s) and not of MDPI and/or the editor(s). MDPI and/or the editor(s) disclaim responsibility for any injury to people or property resulting from any ideas, methods, instructions or products referred to in the content.